

Contents list available at CBIORE journal website

Remarkable Energy Development

Journal homepage: https://ijred.cbiore.id



Research Article

A dry cold sintering to Ta doped-lithium lanthanum zirconate solid electrolyte for all-solid-state lithium metal battery

Fitria Rahmawati^{1*}, Imam S. Alaih², Azka W. Rosalin¹, I.F. Nurcahyo¹, Hartoto Nursukatmo³, Hanida Nilasary³, Haryo S. Oktaviano³, Edo Raihan³, Soraya U. Muzayanha³, Muhammad F. A. Handaka³

¹Chemistry Department, Faculty of Mathematics and Natural Sciences, Sebelas Maret University, Jl. Ir Sutami 36 A Kentingan 57126, Surakarta, Indonesia

Abstract. Solid electrolyte is the essential part in all-solid-state battery (ASSB), in which the sintering step is vital to get a dense and high ionic conductivity. However, Li-loss frequently occurs at a high temperature, causing ionic conductivity to drop. This research investigated a dry-cold sintering process (dry-CSP) to Ta doped-LLZO (LLZTO), in which the LLZTO powder was pressed by cold isostatic pressing (CIP) at 40 MPa without solvent addition and then heated at 300oC for 2h. XRD analysis found that LLZTO300C40P remains crystallized in a single cubic with ionic conductivity of (3.02⊠ 0.53) x 10-5 Scm⁻¹, which is higher than another result in Al doped-LLZO by CSP uniaxial pressing and with moistened-solvent (wet-CSP). The feasibility was tested by preparing a coin cell with a LiCoO₂ cathode and Li metal anode. Cyclic voltammogram of the LCO-LLZTO300C40P-Li ASSB provides a high current density representing a higher electrochemical reaction rate inside the full cell. The battery ran well with an initial charging capacity of 88 mAh/g, and a discharge capacity of 50 mAh/g, providing 56.8 % Coulombic Efficiency. An interface engineering between electrode-solid electrolyte is essential to develop the ASSB performance.

Keywords: dry cold sintering, lithium lanthanum zirconate, Tantalum doped-LLZO, solid electrolyte, all solid state-lithium- ion battery



@ The author(s). Published by CBIORE. This is an open access article under the CC BY-SA license (http://creativecommons.org/licenses/by-sa/4.0/).

Received: 16th May 2024; Revised: 28th July 2024; Accepted: 2nd August 2024; Available online: 12th August 2024

1. Introduction

Research on lithium-ion batteries with solid electrolyte is recently developed fast due to solid electrolytes providing more safety, stability, and no leakage possibility (Ma and Chi, 2016). Lithium lanthanum zirconate, Li₇La₃Zr₂O₁₂ (LLZO), is a prevalent garnet-type solid electrolyte because of its high energy density and a vast potential window > 5V versus Li/Li⁺ (Li *et al.*, 2019; Pazhaniswamy *et al.*, 2023) and also provides high ionic conductivity at around $10^{-3} - 10^{-2}$ Scm⁻¹, which is sufficient for solid-state battery (Zhang et al., 2016). It is found that the cubic garnet LLZO has higher ionic conductivity than the tetragonal phase. The cubic structure can be stabilized by a small amount of doping of some elements such as Ta, Al, Ga, Nb, Te (Deviannapoorani *et al.*, 2015).

Sintering treatment is an important process to densify and increases the ionic conductivity. LLZO based-electrolyte i.e., Li_{6.61}La₃Zr₂Al_{0.13}O_{11.98} which was sintered at 1100 °C 3 h provides a high ionic conductivity of 1.35 x 10⁻⁴ Scm⁻¹ (Padarti *et al.*, 2018). However, another research on Ta doped-LLZO or LLZTO with non-stoichiometric formula of Li_{6.28}La₃Zr_{1.75}Ta_{0.25}O₁₂, found that sintering at 1100 °C for 4h resulting resistive phase of La₂Zr₂O₇, and when 10% Li excess was added by LiOH addition followed by further heating at 1100 °C 16 h, the resistive phase was

disappeared, however, the ionic conductivity of the produced-LLZTO is low, i.e., 7.0 x 10⁻⁶ Scm⁻¹ (Zhang and Fergus, 2017). Low density of the sintered-LLZTO was mentioned as the reason for this such low ionic conductivity (Zhang and Fergus, 2017), however, Li-loss during high temperature treatment could be another reason, because lithium oxide, Li₂O sublimates at temperature above 1000°C, and thus combine with long time sintering brings about a serious Li-loss problem (Huang et al., 2019; Murugan et al., 2008) which reduce the Li-ion conductivity (Shin et al., 2015). Therefore, 5% to 10% lithium salt such as Li₂CO₃ is usually added to overcome the Li loss during calcination (Barai et al., 2021). Some researchers added synthesis-powder as the mother powder for sintering (Xu et al., 2016; Xue et al., 2018; Yang et al., 2020; Yoon et al., 2017). The Li excess addition during synthesis will increase cost once mass production is planned.

To overcome the Li loss problem, some researchers used low-temperature sintering, such as for Al doped-LLZO that was sintered at 900 °C resulted in high ionic conduction of 2.11 x 10⁻⁴ Scm⁻¹ at room temperature (Hu, Z; Liu, H; Ruan, H. B.; Zhang, 2016). The high ionic conductivity indicates that the Li loss did not occur at 900 °C without the mother powder applied during

²Department of Materials Engineering and Convergence Technology, Gyeongsang National University, Jinju, Gyeongnam 52828, South Korea

³R&D Refinery - PT. PERTAMINA (Persero), Jl. Raya Bekasi Km. 20 Pulogadung Jakarta Timur 13920, Indonesia

^{*} Corresponding author Email: fitria@mipa.uns.ac.id (F. Rahmawati)

sintering. Removing the mother powder from the synthesis procedure is another advantage regarding the cost of synthesis. Some metal oxides were also prepared by cold sintering process (CSP), which combines uniaxial pressing with the lowtemperature treatment of 300 °C (Galotta and Sglavo, 2021; Maria et al., 2017). However, less research investigated CSP for LLZO-based-solid electrolytes (Seo et al., 2020; Wang et al., 2020). In the CSP method, the material is moistened with a solvent such as water or acid solution (Wang et al., 2020) and a polymer-salt solvent (Seo et al., 2020). The transient liquid solvent drives the atomic process allowing the dissolutionprecipitation process to densify the ceramic materials at low temperatures (Funahashi et al., 2017; H. Guo et al., 2016; Wang et al., 2020). However, despite the dissolution-precipitation, some elements, which are Li and Al in the case of Al doped-LLZO, preferentially dissolved into the solvent and produced a transient liquid phase deviated from stoichiometric LLZO (Wang et al., 2020). Similar issue with CSP to BaTiO₃ (J. Guo et al., 2016). The incongruent dissolution caused precipitation of the intergranular phase, such as β-Li₅AlO₄ in the case of Al-doped LLZO (Wang et al., 2020), instead of pure LLZO. Although the intergranular phase contributes to LLZO densification, the ionic conductivity is very low and then degraded total conductivity significantly.

Meanwhile, considering material densification, cold isostatic pressing (CIP) is a good alternative for uniaxial pressing. as frequently used in CSP (Seo et al., 2020; Wang et al., 2020). In uniaxial pressing, the pressure is applied in a single axial direction; meanwhile, isostatic pressing applies the pressure uniformly in all directions. It results in technical values 15% superior to those achieved with mono or bi-axial pressing (Concept, 2023). Furthermore, CIP can increase the contact area between grains, increase grains size, and reduce pore size, leading to faster ionic transfer within the solid electrolyte (Afyon et al., 2019). Previous research on Li7La3Zr2O12 found that applying CIP at 60 MPa followed by sintering at 900 °C for 3 h provides 1.35 x 10⁻⁴ Scm⁻¹ (Padarti et al., 2018). Therefore, trying a combination of cold sintering temperature (300 °C) with CIP will be challenging. In addition, the problem with the transient liquid solvent, as found previously (Wang et al., 2020), might be overcome by pressing in all directions with CIP instead of using a solvent to promote dissolution-precipitation. This research aims to investigate a dry cold sintering process (dry-CSP) that combine low temperature heat treatment of 300 °C with cold isostatic pressure of 40 MPa to densify LLZTO solid electrolyte. The result was compared with a high temperature treatment of 900 °C and 40 MPa of CIP. Feasibility of both solid electrolytes, the LLZTO300C40P and the LLZTO900C40P were tested in a full cell with LiCoO2 cathode and Li metal anode.

2. Experiment

2.1. Preparation of LLZTO green pellets and the densification

Ta doped-LLZO was procured from China (GL Advanced Materials Ltd., China). The powder was analyzed by XRD (Rigaku Miniflex 600) equipped with Le Bail refinement using Rietica software (a free edition) to understand the phases, crystal structure, and cell parameters. The LLZTO powder. The LLZTO powder (1 g) was poured into a die press and then hydraulically pressed at 5 tons for 10 min to produce a green pellet, followed by CIP at 40 MPa. Next, the pellet was sintered at 300 oC for 2 h to produce LLZTO-300C40P. Another treatment was also applied by firing the LLZTO green pellet at 900 oC 12 h without mother powder, according to previous research (Hu, Z; Liu, H; Ruan, H. B.; Zhang, 2016).

The sintered pellets were then characterized by XRD (Rigaku Miniflex 600) to understand the phases and crystal structure, SEM/EDX (FEI Inspect-S50) analysis to understand its surface morphology and elemental analysis. Silver blocking-impedance analysis by LCR meter EUCOL CS-150, 20 Hz $-5\,$ MHz

2.2. Fabrication of all solid-state battery LiCoO2-LLZTO-Li metal

The full cells of LiCoO₂ (LCO)-LLZTO300C40P-Li and LCO-LLZTO900C-Li were assembled within stainless steel glove box (VGB-1, ultra-high pure Argon gas, Vacuum level -0,1 MPa). LCO slurry was made by dispersing LiCoO₂ powder (Sigma Aldrich), acetylene black (PT KGC Saintifik, Indonesia), and PVdF (EQ-Lib-PVDF) at a weight ratio of 80 %: 10%: 10%. N-methyl 2- Pyrrolidone (NMP, PT KGC Saintifik Indonesia) was used as a binder. The cathode slurry was stirred for 1 h and then applied to the LLZTO surface. After drying at room temperature, the LCO-LLZTO was weighed to know the cathode active mass. The LLZTO pellet was heated at 180 °C within the VGB, and then the Li metal was attached to the hot LLZTO surface. After cooling for 5 minutes, the LCO-LLZTO-Li was packed within coin cell CR2032 and tightened by a crimper machine (TMAXCN at 1000 Psi).

The full cell LCO-LLZTO-Li was analyzed by cyclic voltammetry (Corrtest CS-150) in between (-4) - 5 V vs. Li/Li⁺ and 1 mVs⁻¹ of scanning rate. Meanwhile, charge-discharge test was conducted by NEWARE Battery Testing System (5A1V) under 0.1mA current drawn, to understands the specific capacity (mAh.g⁻¹) and the Coulombic Efficiency (%).

2.3. Data Analysis

XRD pattern of LLZTO was compared with a standard diffraction of cubic LLZO from Inorganic Crystal Structure Database (ICSD) to identify some specific cubic garnet major peaks at 2θ of 26° , 31° , and 34° , and some minors. The diffraction pattern was also refined with RIETICA to understand the crystal structure, crystal parameters, % mole of identified phases such as cubic and tetragonal phases, the residual phase (Rp), and the residual weight phase (Rwp). Morphological analysis by SEM informed the grain form and size, and the availability of voids.

The impedance measurement resulted real impedance, Z' (Ohm) and phase angle, θ . The data was analyzed by calculating imaginary impedance, Z' (Ohm). A Nyquist plot was made by plotting real impedance, Z', to imaginary impedance, Z''. The Nyquist plot was then fitted by ZView software (a software embedded in Corrtest CS-150 Electrochemical workstation) by applying a resistor-capacitor, RC, networks. The resistance value found by fitting was then used to calculate conductivity (σ) by equation (1), with resistance R (Ohm), pellet thickness I (cm), and surface area of active electrode I' (Nishihora et al., 2018; Rahmawati et al., 2019).

$$\sigma = \frac{1}{R} \frac{l}{A} \tag{1}$$

Charge-discharge test of the prepared-ASSB resulted specific charging capacity (mAh/g) and a specific discharge capacity (mAh/g) at every cycle. Coulombic efficiency was calculated by equation (2).

$$\eta = \frac{\text{specific discharge capacity } (\frac{mAh}{g})}{\text{specific charge capacity } (\frac{mAh}{g})} \times 100 \text{ (\%)}$$
 (2)

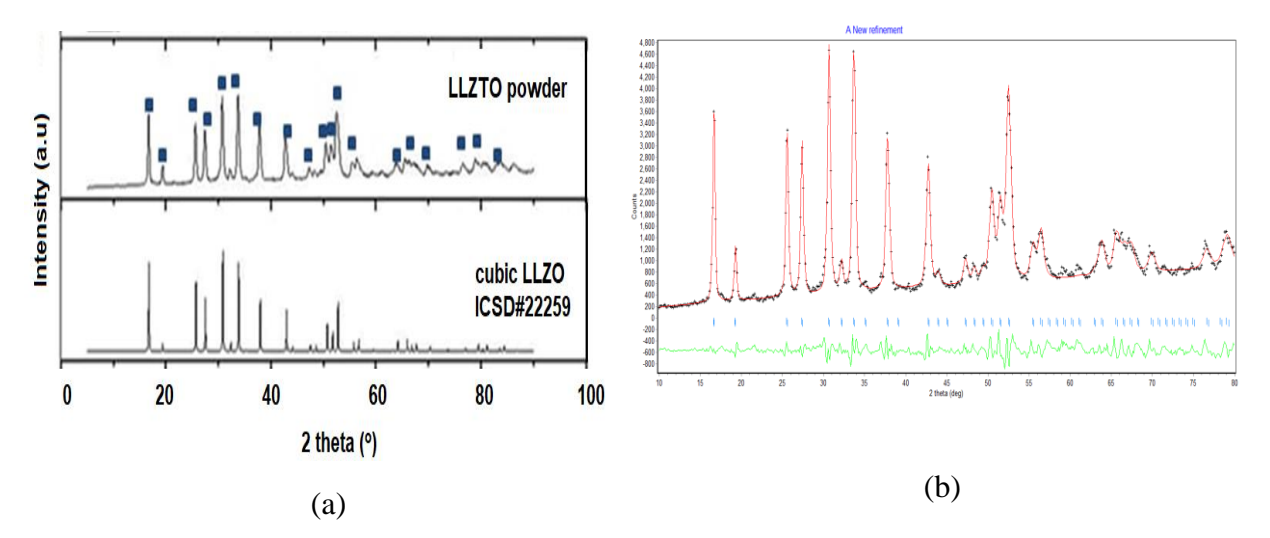


Fig 1. (a) XRD patterns of the LLZTO powder compared with the standard diffraction of cubic garnet LLZO ICSD#422259, and (b) its Le Bail plot by submitting cubic structure and space group of Ia-3d.

3. Result and Discussion

3.1. Characterization of LLZTO powder

XRD analysis of the procured powder found that the powder is fully cubic with all the characteristic peaks matching well with cubic garnet LLZO ICSD#422259 as shown by Fig.1(a) along with its Le Bail plot (Fig.1(b)). Le Bail refinement found that the LLZTO powder is in a single cubic structure with a space group of I a -3 d. In the residual phase, Rp is 6.16 %, and in the residual weight phase, Rwp is 6.10 %. The cell parameters are a=b=c = 13.0334 Å. It is known that until recently LLZO based-materials are available within three structures of high temperature (HT), i.e., cubic with Ia-3d (Awaka *et al.*, 2011), tetragonal structure with I41/acd space group(Awaka *et al.*, 2011), and the low temperature (LT) cubic (Xie *et al.*, 2011) as found within this LLZTO research.

SEM analysis found that the powder consists of round shape aggregates (Fig.2(a)). Meanwhile, EDX mapping analysis shows the powder composition of La, Zr, Ta, and O with the weight percentage of each, as depicted in Fig 2(b). Unfortunately, the Li did not reveal due to Li being a very light

element that EDX cannot detect. Meanwhile, $0.2\,\%$ weight of Al is present as an impurity.

3.2. Characterization of LLZTO300C40P and LLZTO900C40P

The XRD pattern of the sintered LLZTO is depicted in Figure 3 compared with the XRD pattern of LLZTO powder. The patterns show that 40 MPa CIP and 300 °C 2 h did not change the cubic structure of the LLZTO. The LLZTO300C40P characteristic peaks are less intense than the LLZTO powder (Fig 3) because LLZTO300C40P was in sintered-pellet form when analysed. Sintering temperature of 900 °C allowed some tetragonal peaks revealed at 2θ of 16.97° ; 19.61° ; 25.91° and 57.77°, indicate that heat treatment reverses the cubic room temperature into tetragonal. Such a reversible transition from tetragonal to cubic and cubic to tetragonal has also been found when Ga doped-LLZO is co-doped by Sr at a definite Sr amount. The transformation route starts when the lattice parameter increases until it reaches the tetragonal phase (Raju et al., 2021). A similar parameter increasing is also found in this research when LLZTO-40P was fired at 300 °C, as shown in Table 1, the parameter increases from 13.048961 Å into 13.210393 Å, and firing at 900 °C transformed 50.35 % cubic structure into

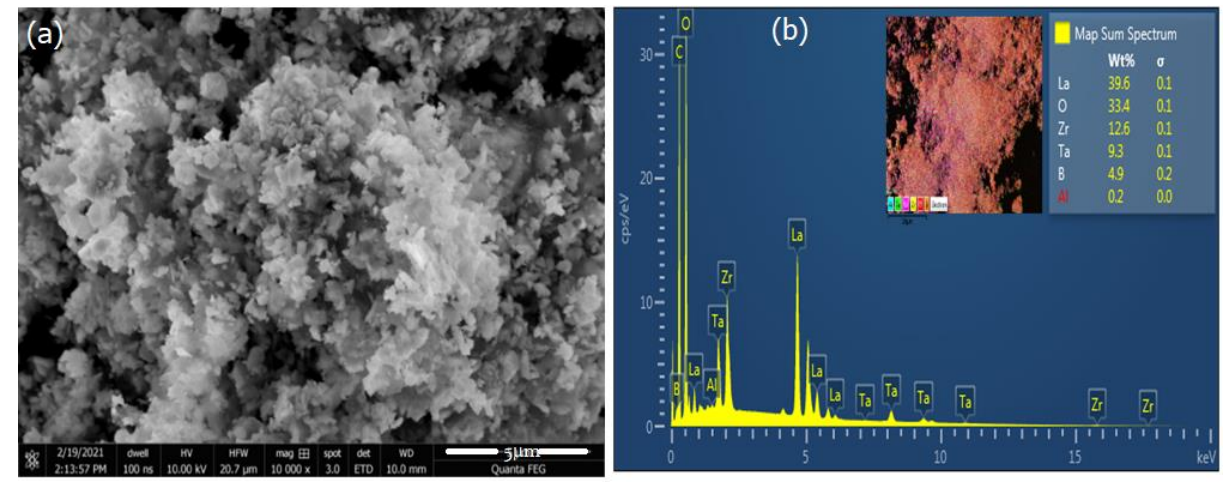


Fig 2. (a) The SEM image, and (b) the EDX mapping of the LLZTO powder

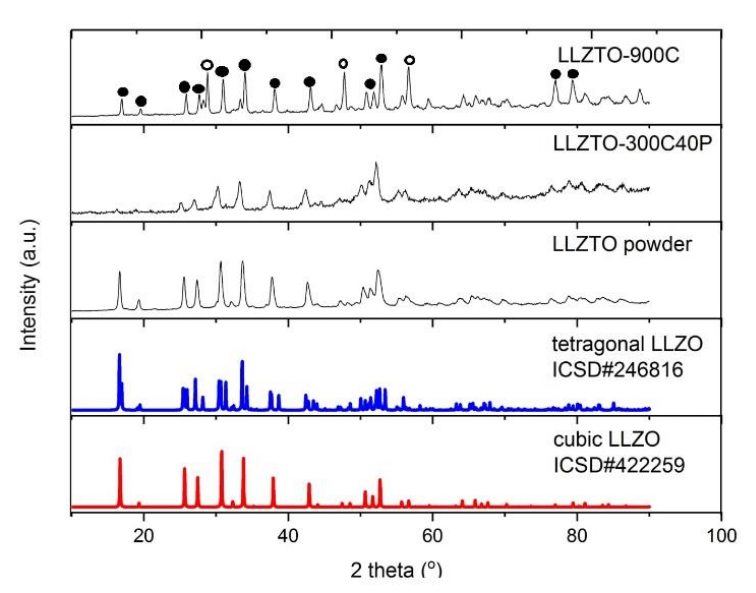


Fig 3. XRD patterns of LLZTO powder, LLZTO-300C40P, LLZTO-900C compared with standard diffraction of cubic LLZO ICSD#422259 and tetragonal LLZO ICSD#246816. The ● sign refers to the cubic phase, and the o sign refers to the tetragonal phase.

Refinement result of LLZTO powder, LLZTO-300C40P and LLZTO-900C40P by submitting cubic and tetragonal structure

	LLZTO	LLZTO-300C40P	LLZTO-900C40P		
Structure/	Cubic/	Cubic/	Cubic/	Tetragonal /	
space group	I a -3 d	I a -3 d	I a -3 d	I 41/acd	
A (Å)	13.048961	13.210393	12.778399	13.023226	
B (Å)	13.048961	13.210393	12.778399	13.023226	
C (Å)	13.048961	13.210393	12.778399	12.475052	
$\alpha = \beta = \gamma$ (°)	90	90	90	90	
% mole	100	100	49.65	50.35	
Rp (%)	5.55	6.11	5.31		
Rwp(%)	3.11	9.82		8.65	

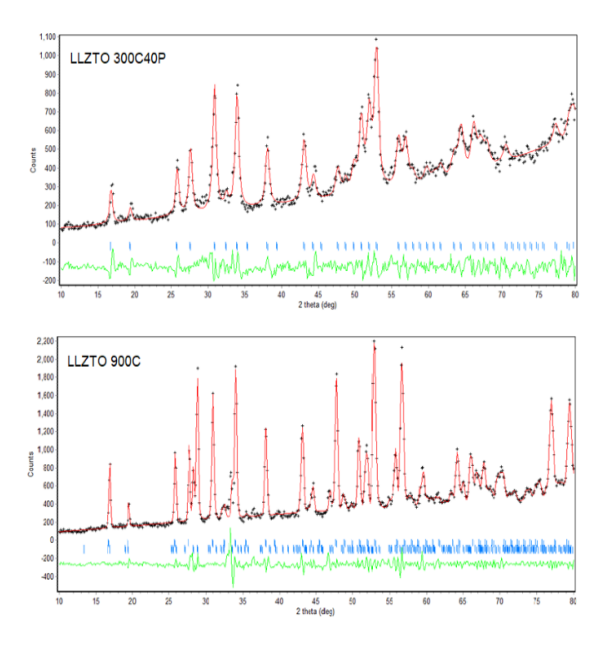


Fig. 4 Le Bail plots of LLZTO-300C40P, and LLZTO-900C. The black line is the data, and the red line is the calculated line, the blue line is the simulated line, the green line is the difference between the data and the calculation.

tetragonal as confirmed by Le Bail refinement (Table 1). The refinement proceeded well when the second phase, a tetragonal structure according to ICSD#246816, was submitted into the calculation.

The Le Bail plot is depicted in Fig 4(b), where most of the peaks were calculated well, leaving residual factors of 5.31% and 8.65% of Rp and Rwp, respectively. It is interesting to be further studied because other research on sintering temperature mostly correlates the temperature's effect to the density and ionic conductivity (Barai *et al.*, 2021; Xue *et al.*, 2018) without discussing the impact on lattice parameters.

As shown in Figure 5, SEM images confirm that 300°C has only slightly sintered the grains, but apparently, it sufficiently compacted the powder resulting in fewer voids available. Meanwhile, the 900°C heating could sinter the pellets, shown by larger grains than before sintering, as described in Figure 5(d). However, the aggregation incongruently occurred, providing some voids available. Figure 5(d) also shows glassy phases formed between grains. The voids and glassy phases could limit the transport of Li ions from grain to grain, leading to lower ionic conduction (Guo *et al.*, 2019; Seo *et al.*, 2020). It is confirmed by impedance measurement, as shown in Fig. 6, in which LLZTO900C provides a much larger impedance curve than LLZTO300C40P. ZView fitting to the impedance data produces Bode plots along with their R-C network, as described in Fig. 6.

Figure 6 shows that LLZTO300C40P has a semicircle like the LLZTO900C. Individual plot of LLZTO300C40P along with

Table 2
The ionic conductivity of LLZTO300C40P compared with other CSP results

The folial conductivity of EEZ 1 0500C401 compared with other CS1 results						
Materials	R_{ionic} (k Ω)	Capacitance (F)	Sintering method	Ionic conductivity (Scm ⁻¹) and temperature	Reference	
Sr-Mg doped-LLZO			Wet CSP DMF solvent	2.6 x 10 ⁻⁵ @40°C	(Seo et al., 2(Seo et	
Al doped-LLZO Li _{6.1} Al _{0.3} La ₃ Zr ₂ O ₁₂			Uniaxial pressing Wet CSP water and HNO ₃ solvent Uniaxial pressing	3.38 x 10 ⁻⁹ @RT	al., 2020) (Wang et al., 2020)	
LLZTO300C40P	52.15	2.13x10 ⁻⁸	Dry CSP isostatic pressing	(3.20±0.53) x 10 ⁻⁵ @RT	This research	
LLZTO900C	1795	1.09 x 10 ⁻⁹	Dry CSP isostatic pressing	1.76 x 10 ⁻⁶ @RT	This research	

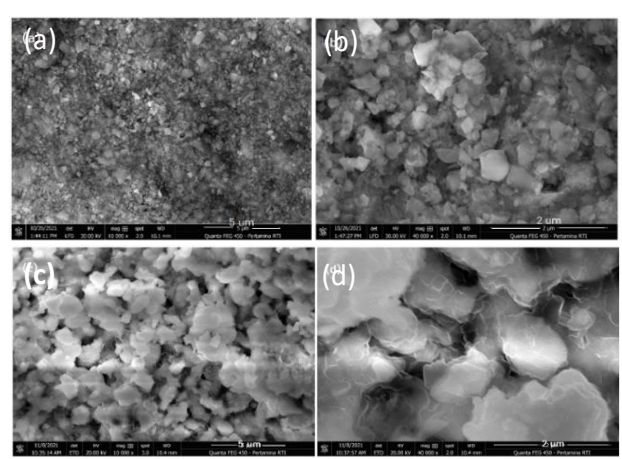


Fig. 5 SEM images LLZTO-300C40P (a)(b), and LLZTO-900C40P (c)(d) at different magnification

its fitting plot and the R-C network is inserted in Fig. 6. The Nyquist plot was fitted with a double R-C network in accordance with two semicircle available for LLZTO300C40P. Both impedance curves differ from previous research finding a semicircle along with a tail at low frequency (X. Zhang *et al.*, 2019). The previous research scanned the impedance at 0.5 - 30 MHz(X. Zhang *et al.*, 2019); this research measured at 20 - 5

MHz. The bottom frequency needs to be expanded below 20 Hz. The low frequency confirms Warburg diffusion (Yang et al., 2020). Meanwhile, high frequency shows ionic transport within the crystal structure. Table 2 shows ionic resistance resulting from ZView fitting along with their capacitance. Constant Phase Element, CPE, was used in parallel connection with Resistor, R, as described by the inserted model in Fig.6. Both capacitance values are between 10⁻⁸ – 10⁻⁹F, indicating ionic migration within a grain or grain conduction. Capacitance up to 0.1 pF or 1 x 10⁻¹ ¹¹ F shows grain resistance (Martin et al., 2007; Rahmawati et al., 2012) or defined capacitance between 10⁻⁸ - 10⁻¹¹ F refers to grain resistance (García-Sánchez et al., 2003; Rahmawati et al., 2021). Table 2 shows that LLZTO300C40P has an ionic conductivity of (3.02 \pm 0.53) x 10⁻⁵ Scm⁻¹ at room temperature (RT), which is higher than the ionic conductivity of the solid electrolyte with the formula of $Li_{0.5x}La_{0.5x}Zr_{1-x}O_{12-d}$, i.e., 1.03 x 10 ⁵ Scm⁻¹ (Arifah *et al.*, 2022), and Li_{6,03}La₃Zr_{1,533}Ta_{0,46}O₁₂ that was sintered at 1000 °C 12 h, i.e., 5.21x10⁻⁶ Scm⁻¹ (Abreu-Sepúlveda et al., 2016). Even though the $Li_{6.03}La_3Zr_{1.533}Ta_{0.46}O_{12}$ has a single cubic garnet structure, a 1000 °C 12 h seems to produce some minor impurities. The minor impurities were also founded within $Li_7La_3Zr_{1.4}Ti_{0.6}O_{12}$, which was sintered at 950 °C12 h and resulting only 1.01 x 10⁻⁶ Scm⁻¹ (Abreu-Sepúlveda et al., 2015). The ionic conductivity of LLZTO300C40P is also higher than Al doped-LLZO (Li_{6.1}Al_{0.3}La₃Zr₂O₁₂), with wet-CSP treatment under 350 MPa uniaxial pressure, with ionic conductivity far below high sintered-LLZO, i.e., 3.38 x 10-9 Scm-1 (Wang et al., 2020).

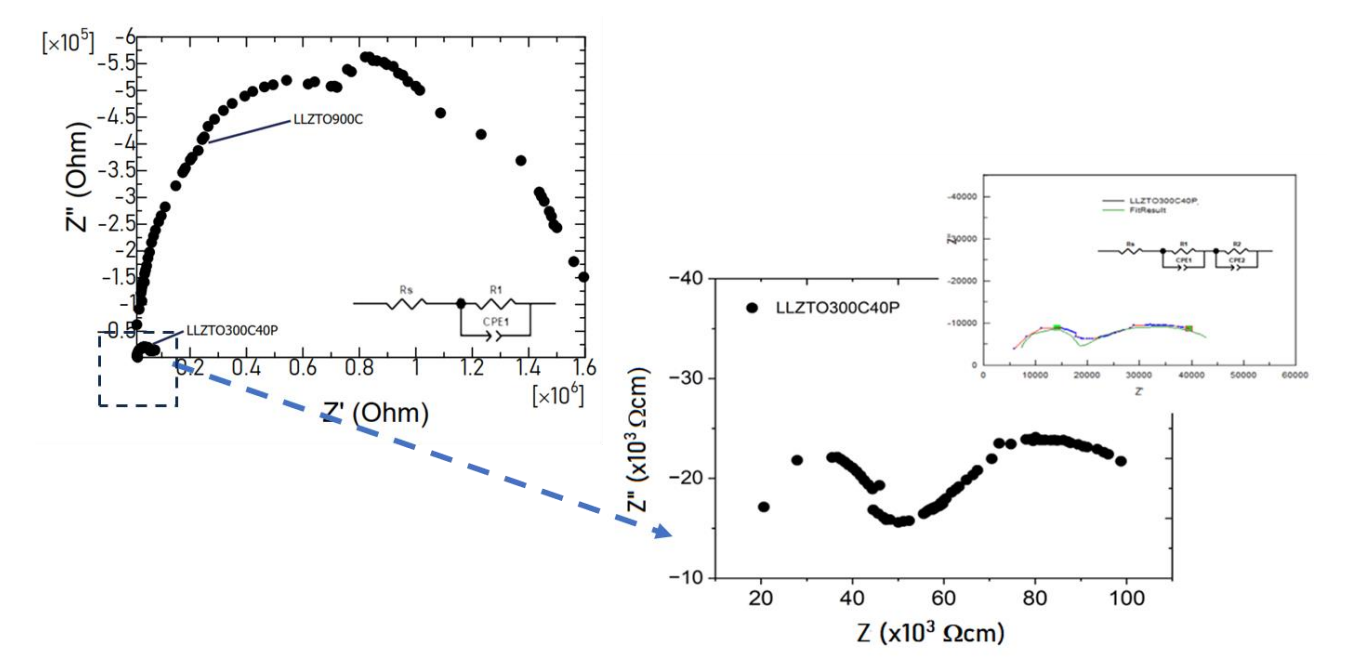


Fig 6. Nyquist plot of LLZTO300C40P and LLZTO900, along with R-C network for ZView fitting

The ionic conductivity of LLZTO300C40P is also slightly higher than Sr-Mg-doped-LLZO with Dimethyl formamide as moistened solvent and uniaxial pressing of 400 MPa. The ionic conductivity is 2.6 x 10⁻⁵ Scm⁻¹ at 40 °C (Seo *et al.*, 2020). Table 2 provides ionic resistance ($R_{\rm ionic}$), Capacitance (F), ionic conductivity (Scm⁻¹), and some previous results on LLZO-based material sintered by the CSP method. Table 2 also shows that LLZTO900C provides ionic conductivity of 1.76x10⁻⁶ Scm⁻¹. Those findings confirm that sintering treatment is an essential parameter in solid electrolyte preparation instead of just concern about crystal structure. Because even though the material was crystallized into single cubic, when heat treatment was applied, Li loss, some minor or secondary phases may occur and decrease the ionic conductivity of the material.

3.3. The electrochemical performance of ASSB with LLZTO300C40P and LLZTO900C40P solid electrolyte

Cyclic voltammetry analysis of LCO-LLZTO300C40P-Li and LCO-LLZTO900C-Li produced voltammogram as described in Fig.7. The result shows that both batteries show a reversible reaction, in which the LLZTO300C40P battery provides one order higher current density than LLZTO900C indicates higher redox reaction rate. The higher ionic conductivity of LLZTO300C40P, as shown in Table 2, contributes significantly to the battery performance. The reaction reversibility proves the rechargeable ability of the prepared batteries.

Fig.7 shows onset potential at 0.3 V vs. Li+/Li (2.74 V vs. SHE) and reaching peak potential of 2 V vs Li/Li+, and onset reduction potential at 0.3 V vs. Li+/Li (-2.75 V vs. SHE) flows down to potential peak of -2 V vs Li/Li+, indicating deintercalation and intercalation of Li ions to LCO. Onset potential informs the potential of the analyte starts to oxidise and start to reduce at the electrode surface cause the current to increase exponentially until reaching a peak(Batchelor-McAuley, 2023). The value is almost similar to the CV result of Au-LLZTO-Li, which shows 0 V vs. Li+/Li (3.04 V vs. SHE) according to Li dissolution and Li deposition (Y. Zhang et al., 2019). Another research on LCO-Li solid-state battery Li_{6.75}La₃Zr_{1.75}Nb_{0.25}O₁₂ as a solid electrolyte found a similar oxidation start with a peak at around 3.8 V corresponding to

deintercalation of Li ion into LCO (Guo et al., 2021). Meanwhile, the second peak starts at 3.0 V vs. Li+/Li (0.04 V vs. SHE) climbed to 4.3 V , indicating the dissolution of Ta, which is reversibly deposited, shown by a small second reduction peak under a negative current. The voltammogram also displays a high reduction peak starting at 0.3 V vs. Li+/Li belongs to Li deposition. Compared to LCO-LLZTO900C-Li (blue curve in Fig.7), LCO-LLZTO300C40P-Li provides higher current density, indicating a higher redox reaction rate inside the full cell. The higher ionic conductivity of LLZTO300C40P, as shown in Table 2, significantly support redox reaction within the electrochemical cell and leads to higher battery performance. Fig.7 also shows that the curves have two oxidation-reduction peaks. LLZTO900C shows only one peak at each oxidation and reduction area, confirming Li dissolution and deposition. A second peak also appeared, confirming the secondary reaction, but the response is not reversible back, as one peak only reveals under the reduction area (Fig. 7 (the inserted blue curve)).

To check the feasibility of the LLZTO300C40P, a solidstate battery was fabricated with an LCO cathode and Li metal anode. Charge-Discharge analysis to LCO-LLZTO300C40P-Li shows an initial charging capacity of 88 mAh/g and an initial discharge capacity of 50 mAh/g at room temperature (RT), and it was stable until 10 cycles with Coulombic efficiency around 64% (Fig.8). The result is better than previous research on all solid-state Li metal batteries with Nb doped-LLZO (Li_{6.75}La₃Zr_{1.75}Nb_{0.25}O₁₂) solid electrolyte and LCO cathode, which found a discharge capacity of only 20 – 30 mAh/g at 100 °C. After modifying the cathode-electrolyte interface by attaching Al₂O₃ film on the LCO surface, the specific capacity increases to 193.6 mAh/g at 100 °C and becomes stable after 16 cycles at 76 mAh/g (Guo et al., 2021). Therefore, it is essential to engineer the interface between LLZTO300C40P and the cathode or anode in the future.

4. Conclusion

A solid electrolyte preparation through a dry-CSP by combining 40 MPa cold isostatic pressing and 300 °C heating for 2 h under air without mother powder has produced a solid electrolyte with ionic conductivity of (3.02± 0.53) x 10⁻⁵ Scm⁻¹ at RT, which is

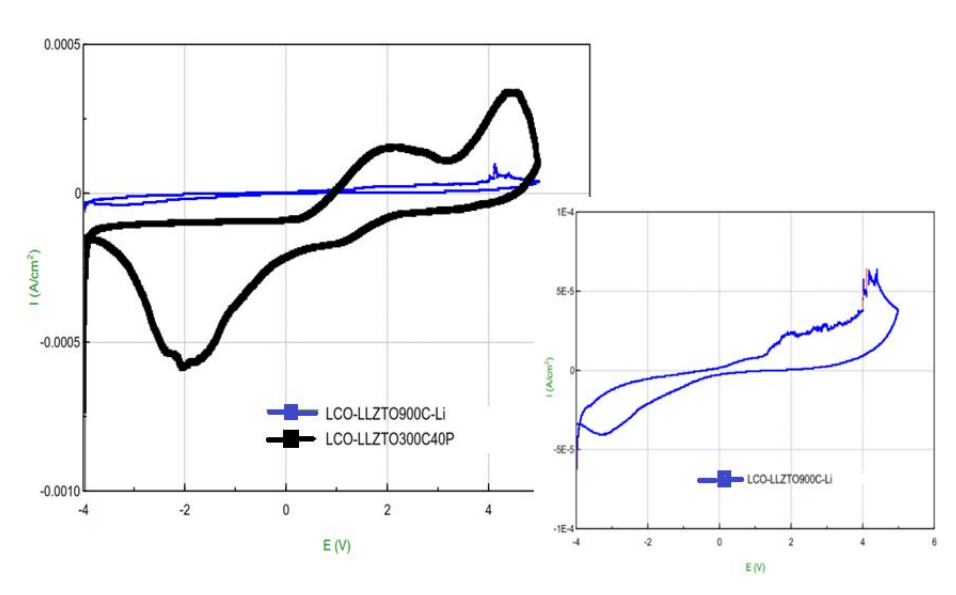
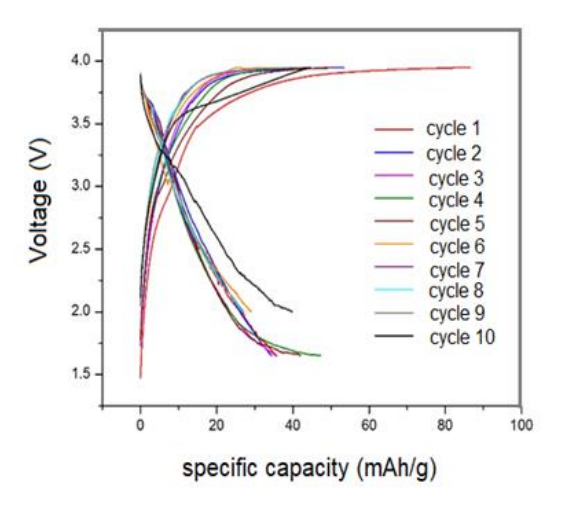


Fig 7. Cyclic voltammogram of LCO-LLZTO 300C40P-Li and LCO-LLZTO900C-Li at a scanning rate of 1 mV/s within -4 to 5 V vs. Li/Li⁺. The black line curve refers to LCO-LLZTO300C40P-Li, and the blue line curve refers to LCO-LLZTO900C-Li. Inserted is the magnification of the LCO-LLZTO900C-Li curve



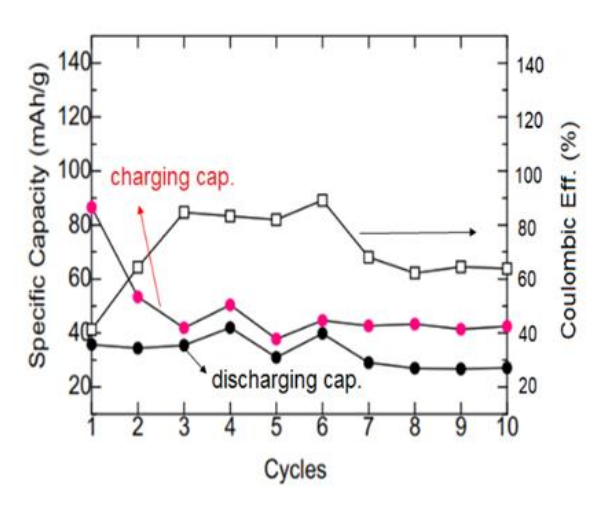


Fig 8. (a) Charge-Discharge Curve and, (b) Coulombic Efficiency (%) of LCO-LLZTO300C40P-Li metal battery

higher than Al doped-LLZO and Sr-Mg doped-LLZO which were sintered by a wet-CSP method. The full cell of LCO-LLZTO300C40P-Li metal shows a cyclic voltammogram with higher current density representing a higher electrochemical reaction rate inside the full cell. Charge-discharge test found an initial charging capacity of 88 mAh/g and a discharge capacity of 50 mAh/g, providing Coulombic Efficiency of 56.8 %. An interface engineering between the electrode with the solid electrolyte LLZTO300C40P is essential to increase the ASSB performance.

Acknowledgement

This research is supported by The Ministry of Education, Culture, Research and Technology, Republic of Indonesia, under a scheme of Penelitian Dasar Perguruan Tinggi (PDUPT) 2021 and 2022, and partly supported by PDSMR Pertamina. The authors acknowledge all the support.

Conflict of interest. On behalf of all authors, the corresponding author states that there is no conflict of interest.

References

Abreu-Sepúlveda, M., Williams, D.E., Huq, A., Dhital, C., Li, Y., Paranthaman, M.P., Zaghib, K., Manivannan, A., 2016. Synthesis and characterization of substituted garnet and perovskite-based lithium-ion conducting solid electrolytes. *Ionics (Kiel)*. 22, 317–325. https://doi.org/10.1007/s11581-015-1556-2

Abreu-Sepúlveda, M., Williams, D.E., Huq, A., Dhital, C., Li, Y., Paranthaman, M.P., Zaghib, K., Manivannan, A., 2015. Synthesis and characterization of substituted garnet and perovskite-based lithium-ion conducting solid electrolytes. *Ionics (Kiel)*. 22, 317–325. https://doi.org/10.1007/s11581-015-1556-2

Afyon, S., Kravchyk, K.., Wang, S., Broek, J., van den, Hänsel, C. Kovalenko, M. V, Rupp, J.L.M., 2019. Building Better All-Solid-State Batteries with Li-Garnet Solid Electrolytes and Metalloid Anodes. J. Mater. Chem. A 7, 21299–21308.

Arifah, S.K., Nugrahaningtyas, K.D., Hidayat, Y., Kim, H., Lee, Y., Rahmawati, F., 2022. Synthesis of a low Li to Zr mole ratio of lithium lanthanum zirconate Li0.5xLa0.5xZr1-xO12-δ. *J. Aust. Ceram. Soc.* https://doi.org/10.1007/s41779-022-00782-7

Awaka, J., Takashima, A., Kataoka, K., Kijima, N., Idemoto, Y., Akimoto, J., 2011. Crystal structure of fast lithium-ion-conducting cubic Li 7La3Zr2O12. *Chem. Lett.* 40, 60–62. https://doi.org/10.1246/cl.2011.60

Barai, P., Fister, T., Liang, Y., Libera, J., Wolfman, M., Wang, X., Garcia, J., Iddir, H., Srinivasan, V., 2021. Investigating the Calcination and Sintering of Li7La3Zr2O12(LLZO) Solid Electrolytes Using Operando Synchrotron X-ray Characterization and Mesoscale Modeling. *Chem. Mater.* 33, 4337–4352. https://doi.org/10.1021/acs.chemmater.0c04393

Batchelor-McAuley, C., 2023. Defining the onset potential. *Curr. Opin. Electrochem.* 37, 101176.

https://doi.org/10.1016/j.coelec.2022.101176

Concept, 2023. axial or isostatic pressing. URL

http://www.zirconiaconcept.it/en/axial-or-isostatic-pressing Deviannapoorani, C., Ramakumar, S., Janani, N., Murugan, R., 2015. Synthesis of lithium garnets from La2Zr2O7 pyrochlore. *Solid State Ionics* 283, 123–130. https://doi.org/10.1016/j.ssi.2015.10.006

Funahashi, S., Guo, J., Guo, H., Wang, K., Amanda L. Baker, Kosuke Shiratsuyu, C.A.R., 2017. Demonstration of the cold sintering process study for the densification and grain growth of ZnO ceramics. *J. Am. Ceram. Soc.* 100, 546–553.

Galotta, A., Sglavo, V.M., 2021. The cold sintering process: A review on processing features, densification mechanisms and perspectives. *J. Eur. Ceram. Soc.* 41, 1–17. https://doi.org/10.1016/j.jeurceramsoc.2021.09.024

García-Sánchez, M.F., M'Peko, J.C., Ruiz-Salvador, A.R., Rodríguez-Gattorno, G., Echevarría, Y., Fernández-Gutierrez, F., Delgado, A., 2003. An elementary picture of dielectric spectroscopy in solids: Physical basis. *J. Chem. Educ.* 80, 1062–1073.

https://doi.org/10.1021/ed080p1062 Guo, H., Baker, A., Guo, J., Randall, C.A., 2016. Protocol for Ultralow-

Temperature Ceramic Sintering: An Integration of Nanotechnology and the Cold Sintering Process. *ACS Nano* 10, 10606–10614.

Guo, H., Shen, F., Guo, W., Zeng, D., Yin, Y., Han, X., 2021. LiCoO2/Li6.75La3Zr1.75Nb0.25O12 interface modification enables all-solid-state battery. *Mater. Lett.* 301, 130302. https://doi.org/10.1016/j.matlet.2021.130302

Guo, J., Floyd, R., Lowum, S., Maria, J.-P., DBeauvoir, T., Seo, J.-H., Randall, C., 2019. Cold Sintering: Progress, Challenges, and Future Opportunities. *Annu. Rev. Mater. Res.* 49, 275–295.

Guo, J., Guo, H., Baker, A.L., Lanagan, M.T., Kupp, E.R., Messing, G.L., Randall, C.A., 2016. Cold Sintering: A Paradigm Shift for Processing and Integration of Ceramics. Angew. *Chemie - Int. Ed.* 55, 11457–11461.

Hu, Z; Liu, H; Ruan, H. B.; Zhang, L., 2016. High Li-ion conductivity of Al-doped Li7La3Zr2O12 synthesized by solid-state reaction. Ceram. Int. 42. https://doi.org/10.1016/j.ceramint.2016.04.149

Huang, X., Song, Z., Xiu, T., Badding, M.E., Wen, Z., 2019. Sintering , micro-structure and Li + conductivity of Li 7 - x La 3 Zr 2 - x Nb x O 12 / MgO (x = 0 . 2 - 0 . 7) Li-Garnet composite

- ceramics. Ceram. Int. 45, 56–63. https://doi.org/10.1016/j.ceramint.2018.09.133
- Li, J., Liu, Z., Ma, W., Dong, H., Zhang, K., Wang, R., 2019. Low-temperature synthesis of cubic phase Li7La3Zr2O12 via sol-gel and ball milling induced phase transition. *J. Power Sources* 412, 189–196. https://doi.org/10.1016/j.jpowsour.2018.11.040
- Ma, C., Chi, M., 2016. Novel solid electrolytes for li-ion batteries: A perspective from electron microscopy studies. *Front. Energy Res.* 4, 1–6. https://doi.org/10.3389/fenrg.2016.00023
- Maria, J.P., Kang, X., Floyd, R.D., Dickey, E.C., Guo, H., Guo, J., Baker, A., Funihashi, S., Randall, C.A., 2017. Cold sintering: Current status and prospects. *J. Mater. Res.* 32, 3205–3218. https://doi.org/10.1557/jmr.2017.262
- Martin, P., Carlos Pico, L.., Veiga, L., 2007. Li(4-x)/3Ti(5-2x)/3CrxO4 $(0 \le x \le 0.9)$ spinels: New negatives for lithium batteries. *Solid State Sci.* 9, 521–526.
 - https://doi.org/10.1016/j.solidstatesciences.2007.03.023
- Murugan, R., Thangadurai, V., Weppner, W., 2008. Lattice Parameter and Sintering Temperature Dependence of Bulk and Grain-Boundary Conduction of Garnet-like Solid Li-Electrolytes. J. Electrochem. Soc. 155, A90. https://doi.org/10.1149/1.2800764
- Nishihora, R.K., Rachadel, P.L., Gabriela, M., Quadri, N., 2018. Journal of the European Ceramic Society Manufacturing porous ceramic materials by tape casting A review. *J. Eur. Ceram.* Soc. 38, 988–1001. https://doi.org/10.1016/j.jeurceramsoc.2017.11.047
- Padarti, J.K., Jupalli, T.T., Hirayama, C., Senna, M., Kawaguchi, T., Sakamoto, N., Wakiya, N., Suzuki, H., 2018. Low-temperature processing of Garnet-type ion conductive cubic Li7La3Zr2O12 powders for high performance all solid-type Li-ion batteries. *J. Taiwan Inst. Chem. Eng.* 90. https://doi.org/10.1016/j.jtice.2018.02.021
- Pazhaniswamy, S., Joshi, S.A., Hou, H., Parameswaran, A.K., Agarwal, S., 2023. Hybrid Polymer Electrolyte Encased Cathode Particles Interface-Based Core–Shell Structure for High-Performance Room Temperature All-Solid-State Batteries. Adv. Energy Mater. 13, 2202981. https://doi.org/10.1002/aenm.202202981
- Rahmawati, F., Musyarofah, B., Nugrahaningtyas, K.D., Prasetyo, A., Suendo, V., Haeruddin, H., Handaka, M.F.A., Nilasari, H., Nursukatmo, H., 2021. A different zirconia precursor for Li7La3Zr2O12 synthesis. *J. Mater. Res. Technol.* 15, 2725–2734. https://doi.org/10.1016/j.jmrt.2021.09.064
- Rahmawati, F., Prijamboedi, B., Soepriyanto, S., Ismunandar, 2012. SOFC composite electrolyte based on LSGM-8282 and zirconia or doped zirconia from zircon concentrate. *Int. J. Miner. Metall. Mater.* 19, 863–871. https://doi.org/10.1007/s12613-012-0640-0
- Rahmawati, F., Zuhrini, N., Nugrahaningtyas, K.D., Arifah, S.K., 2019. Yttria-stabilized zirconia (YSZ) film produced from an aqueous nano-YSZ slurry: preparation and characterization. *J. Mater. Res. Technol.* 1–10. https://doi.org/10.1016/j.jmrt.2019.07.054
- Raju, M.M., Altayran, F., Johnson, M., Wang, D., Zhang, Q., 2021. Crystal Structure and Preparation of Li7La3Zr2O12 (LLZO) Solid-State Electrolyte and Doping Impacts on the Conductivity: An Overview. *Electrochem*. https://doi.org/10.3390/electrochem2030026

- Seo, J.-H., Nakaya, H., Takeuchi, Y., Fan, Z., Hikosaka, H., Rajagopalan, R., Gomez, E., Iwasaki, M., Randal, C., 2020. Broad Temperature Dependence, High Conductivity, and Structure-Property Relations of Cold Sintering of LLZO-based Composite Electrolytes. *J. Eur. Ceram. Soc.* 40, 6241–6248. https://doi.org/10.1016/j.jeurceramsoc.2020.06.050
- Shin, D., Oh, K., Kim, K., Park, K.-Y., Lee, B., Lee, Y.-G., Kang, K., 2015. Synergistic multi-doping effects on the Li7La3Zr2O12 solid electrolyte for fast lithium ion conduction. Sci. Rep. 18053.
- Wang, X., Wang, J., Li, F., Zhu, F., Ma, C., 2020. Influence of cold sintering process on the structure and properties of garnet-type solid electrolytes. *Ceram. Int.* 46, 18544–18550. https://doi.org/10.1016/j.ceramint.2020.04.160
- Xie, H., Alonso, J.A., Li, Y., Fernández-Díaz, M.T., Goodenough, J.B., 2011. Lithium Distribution in Aluminum-Free Cubic Li7La3Zr2O12. *Chem. Mater.* 23, 3587–3589. https://doi.org/doi.org/10.1021/cm201671k
- Xu, B., Duan, H., Xia, W., Guo, Y., Kang, H., Li, H., Liu, H., 2016. Multistep sintering to synthesize fast lithium garnets. *J. Power Sources* 302, 291–297. https://doi.org/10.1016/j.jpowsour.2015.10.084
- Xue, W., Yang, Y., Yang, Q., Liu, Y., Wang, L., Chen, C., Cheng, R., 2018. The effect of sintering process on lithium ionic conductivity of Li6.4Al0.2La3Zr2O12 garnet produced by solid-state synthesis. *RSC Adv.* 8, 13083–13088. https://doi.org/10.1039/c8ra01329b
- Yang, L., Dai, Q., Liu, L., Shao, D., Luo, K., Jamil, S., Liu, H., 2020. Rapid sintering method for highly conductive Li7La3Zr2O12 ceramic electrolyte. *Ceram. Int.* https://doi.org/10.1016/j.ceramint.2020.01.106
- Yoon, S.A., Oh, N.R., Yoo, A.R., Lee, H.G., Lee, H.C., 2017. Preparation and Characterization of Ta-Substituted Li₇La₃Zr_{2×}O₁₂ Garnet Solid Electrolyte by Sol-Gel Processing. *J. Korean Ceram. Soc.* 54, 278–284
- Zhang, H., Liu, Y., Wang, T., Yang, Y., Shi, S., Yang, G., 2016. Li2ZrO3-coated Li4Ti5O12 with nanoscale interface for high performance lithium-ion batteries. *Appl. Surf. Sci.* 368, 56–62. https://doi.org/10.1016/j.apsusc.2016.01.244
- Zhang, X., Fergus, J., 2017. Phase Content and Conductivity of Aluminum- and Tantalum-Doped Garnet-Type Lithium Lanthanum Zirconate Solid Electrolyte Materials. *ECS Trans.* 77, 509–516. https://doi.org/10.1149/07711.0509ecst
- Zhang, X., Oh, T.-S., Fergus, J.W., 2019. Densification of Ta-Doped Garnet-Type Li 6.75 La 3 Zr 1.75 Ta 0.25 O 12 Solid Electrolyte Materials by Sintering in a Lithium-Rich Air Atmosphere . *J. Electrochem. Soc.* 166, A3753–A3759. https://doi.org/10.1149/2.1031915jes
- Zhang, Y., Deng, J., Hu, D., Chen, F., Shen, Q., 2019. Electrochimica Acta Synergistic regulation of garnet-type Ta-doped Li 7 La 3 Zr 2 O 12 solid electrolyte by Li b concentration and Li b transport channel size. *Electrochim. Acta* 296, 823–829. https://doi.org/10.1016/j.electacta.2018.11.136



© 2024. The Author(s). This article is an open access article distributed under the terms and conditions of the Creative Commons Attribution-ShareAlike 4.0 (CC BY-SA) International License (http://creativecommons.org/licenses/by-sa/4.0/)